Gas sensitization and photochromism of $CaTiO_{3-\delta}$ for visible-light photocatalysis

*Jingwen Chen [a], Chong Wang [a], Jibiao Li [b], Jiupai Ni [a], Yu Tang [a], John T.S. Irvine [a,c], Chengsheng Ni [a]**

a College of Resources and Environment, Southwest University, Chongqing, China, 400715.

b Center for Materials and Energy (CME) and Chongqing Key Laboratory of Extraordinary Bond Engineering and Advanced Materials Technology (EBEAM), Yangtze Normal University, Chongqing 408100, China.

c College of Chemistry, University of St Andrews, North Haugh, Scotland, KY16 9ST.

** Corresponding author: nichengsheg@swu.edu.cn*

Abstract: A wide bandgap $CaTiO_{3-\delta}$ (CTO) with oxygen vacancy (V_O) was prepared to investigate the sensitization or photochromism caused by the adsorbed gaseous species, and the resultant photocatalytic performance of CTO under visible light. The adsorption of CO_2 was able to produce an intermediate gap state in CTO according to the density-function-theory (DFT) calculations and was found to increase the light absorption peak at 482 nm (A_{482}). During photocatalytic NO oxidation in air, the V_O on the surface could enhance adsorption and further oxidation of NO_2 intermediates. Furthermore, the gas sensitization and photochromism of CTO contributed to the activation of O_2 in dry air. Our findings will help deepen the knowledge about the chemisorption of gaseous species in the electronic structural tunability of semiconductors and the resultant impact on the photocatalytic reaction at the gas/solid interface.

Keywords: CO_2 adsorption; NO removal efficiency; heterojunction; gas sensitization; photochromism; oxygen vacancy;

1.Introduction

Photocatalysis using the widely available sunlight was an effective technology for eliminating highly diluted NO_X in air [1]. Hence, considerable effort has been invested in the development of high-efficiency, low-cost, and high-stability photocatalysts to oxidize NO into nitrate ions (NO_3^-) [2]. Perovskite-type oxides (nominal formulae: ABO_3), for example, have been engineered for multiple applications in selective catalysis and transformation electrocatalysts [3] due to the stable three-dimensional corner-sharing <AO_6> framework, which was advantageous for the transport of hot charge carriers (electron-hole or e^-–h^+ pairs) and could tolerate a large portion of oxygen vacancy (V_O) through cation doping or reduction [4, 5].

$CaTiO_3$ was a typical wide bandgap (E_g) semiconductor (E_g = 3.56 eV) [6], which restricted its absorption of visible light [7], and hence, improving its visible-light absorption (400-700 nm) would be critical to boost the photocatalytic activity under solar light [8]. The hetero-atomic doping and V_O defect engineering were widely employed to alter the electronic structure and band structure of a broad E_g semiconductor for the photocatalysis under a visible-light insolation [9, 10]. For instance, F^- doping decreased slightly the E_g of Sr_2TiO_4 from 3.28 to 3.22 eV [11], whereas the introduction of V_O could effectively reduce the E_g of $LaNi_{0.9}Cu_{0.1}O_3$ from 3.6 to 2.69 eV [12]. Given this, the current study was dedicated to reduce the E_g of $CaTiO_3$ using V_O defect engineering with the aim of improving its photocatalytic activity. Furthermore, the V_O on the surface may increase the adsorption of small molecules onto the photocatalysts. The V_O of an Aurivillius-phase Bi_3TiNbO_9, for instance, has been reported to enhance the photocatalytic CO_2 reduction [13], whereas the oxygen-deficient $La_{1-x}Sr_xCoO_{3-\delta}$ has been reported to store NO_X on its surface [14, 15], thereby contributing to eliminate the very diluted NOx in air [16]. Likewise, the V_Os with positive charge was specified to promote the adsorption of gas, such as CO_2

for the $La_2NiFeO_{6-\delta}$ [17], but they may also be the recombination sites [18] for the hot e^--h^+ pair in photocatalysis.

The interaction of the ubiquitous small gaseous molecules (H_2O, CO_2, NOx *et al.*) with the superficial layer of an semiconductor was stipulated to create an in-gap band and altered the visible light absorption [19], which was analogous to the "sensitization" in the aqueous solution. Indeed, the interaction between the (defective) wide-gap materials and the adsorbed gas was the basis of their gas sensing in terms of electric properties [20]. The sensitization of a semiconductor in an aqueous system involving the adsorption and the charge transfer from the dye to the semiconductor has been extensively explored in the dye-sensitized solar cells [21], photocatalytic pollutant removal from the textile wastewater, and the photocatalytic water splitting [22]. However, the effect of gas-phase sensitization for photocatalysts has scarcely been highlighted to be effective for the air-pollutant abatement, even though the adsorption of small molecules was widely accepted to interact with the inorganic oxides to produce minor charge carriers or surface density of states.

In this work, a $CaTiO_{3-\delta}$ (CTO) with V_O was prepared at 1300 °C in air and the behavior of the adsorbed molecules, such as H_2, H_2O, and CO_2 besides NO/NO_2 under illumination was investigated to explore their effect on the photochromism of CTO, hot charge-carrier transfer, and atmospheric NO oxidation. CO_2 adsorption can result in an intermediate gap state in CTO, which increased the light absorption peak at 482 nm (A_{482}). During the photocatalytic NO oxidation in wet air, the V_O on the surface could promote the adsorption and further oxidation of NO_2 intermediates, however, CO_2 gas sensitization and photochromism were beneficial for the activation of O_2 in dry air. Annealing in 5% H_2-Ar (5% H_2) would accelerate the desorption of CO_2 from the CTO surface and therefore induce the photocatalytic

reduction of H_2O in wet air. Furthermore, a Z-scheme junction of CTO with CuO demonstrated an enhanced removal efficiency of NO with photons >450 nm. This work paves a new avenue to understand the photocatalysis on gas/solid interface of defective perovskite and sheds novel light on the gaseous sensitization on solid semiconductors.

2. Materials and methods

2.1. Materials

$CaCO_3$ (99.99%), TiO_2 (99.99%), Fe_2O_3 (99.9%), and CuO (99.5%) from Macklin Chemicals in China were used in this experiment.

2.2. Synthesis of CTO, CTO/Fe_2O_3, and CTO/CuO

Stoichiometric oxide precursors ($CaCO_3$, TiO_2) were sintered in air for 5 h at 1300 ºC after being ground in a mortar. The as-prepared CTO was re-calcined in air at 300, 500, and 700 ºC for 1 h, denoted as CTO-300, CTO-500, and CTO-700, respectively. CTO with X% CuO and Fe_2O_3 (X=0.125,0.25,0.5,1) were ground and calcined at 200, 300, and 400 ºC in air for 1 h, which were denoted as X% CTO/CuO-T and X% CTO/Fe_2O_3-T (T= 200, 300, and 400), respectively. CTH-500 was achieved by reducing CTO powder in 5% H_2 (500 mL·min^{-1}) at 500 ºC for 1 h.

2.3. Characterizations

A powder X-ray diffraction (XRD, X'Pert3 Powder, Netherlands) was used to determine the phase composition. An Ultraviolet-1800 spectrophotometer (Macy, China) with a 100-mm integration sphere was used for diffuse ultraviolet-visible (UV-Vis) reflectance spectroscopy. The electron paramagnetic resonance

(EPR) was measured using a Bruker EMX Plus spectrometer. Fourier transform infrared spectroscopy (FTIR, Perkin Elmer, Germany) and X-ray photoelectron spectroscopy (XPS, Thermo Fisher, USA) equipped with an Al K_α anode (1486.6 eV) were used to study the solid's surface properties. The C 1s peak at a binding energy of 284.8 eV were used to calibrate the XPS results. Diffuse reflectance FTIR spectroscopy (DRIFTS) measurements were performed in situ using a Nicolet iS50 spectrometer (Thermo Fisher, USA.) instrument outfitted with a custom reactor and liquid nitrogen-cooled Hg-Cd-Te (MCT) detector. Representative samples were analyzed using scanning electron microscopy (SEM, Phenom ProX, Netherlands) and Raman spectroscopy (Renishaw, InVia) in ambient air at 150 K. The temperature programmed desorption was carried with flowing air on an adsorption equipment (VDSorb-92i, Vodo, China) coupled with a residual gas analyzer (RGA, QIC-20, Hiden, UK) for the efflux. Thermogravimetric analysis (TGA) was carried out using a thermogravimetric analyzer (TG 209 F3, Tarsus). The as-prepared CTO pellet was cut into a rectangular bar of 3 × 3 × 12 mm for the four-probe direct-current electric conductivity on a high-precision multimeter (Keithley 2100, USA).

2.4. Photocatalytic activity

The NO removal experiment was carried out in a specially designed continuous flow stainless steel reactor with a quartz window and a water-cooling system to keep the reaction temperature at 25 ºC. The CTO powder (0.3 g) was distributed over a glass slide with a diameter of 12 cm after being suspended in 5 mL of ethanol. The CTO coating was dried in air and then sealed in the reactor under a light-emitting diode (LED) lamp (FL, 19-III, 100 W, China) equipped without ($\lambda > 400$ nm) or with filter ($\lambda > 450$ nm) (Figure S2), respectively. Air was used to dilute the standard gas (100 ppm (part per million) NO in Ar) to create a 1 L min^{-1} reactive flow with 1 ppm NO. A NOx analyzer (MIC-600, Erantex Electronics, Shenzhen, China)

was employed for the continuous concentration measurement. For some experiments, the CO_2 in air was partly eliminated by a $Ca(OH)_2$ solution, while the mixed O_2 (99.99% purity) and Ar (99.99% purity) was used to achieve an low [CO_2] close to 0 ppm.

The removal efficiency of NO was defined as η (1):

$$\eta = (1 - C / C^0) \times 100\% \qquad (1)$$

where C and C^0 were [NO] (in ppm) in the outlet stream and the feed stream, respectively.

The ionic selectivity (S_i) was calculated according to the equation (2):

$$S_i = (1 - (C_{NO_2} / (C^0_{NO} - C_{NO}))) \times 100\% \qquad (2)$$

where subscripts NO_2 and NO referred to the concentration of respective gases.

The apparent quantum efficiency (AQE) of the photocatalyst was calculated according to the equation (3):

$$AQE = \frac{N_e}{N_p} * 100\% = \frac{n_{1*}K_1 + n_{2*}K_2 + \cdots}{N_p} \qquad (3)$$

N_e *:* Total number of transferred electrons;

N_p: Number of incident photons; Np was calculated using the light intensity (measured using chroma meter (TES 136, Tawan) divided by a coefficient of 0.017 μmol s^{-1} lm^{-1} since the temperature of the light was found to be 6000 K.

n_1, n_2: Amount of the target product (μmol);

K_1, K_2: Number of transferred electrons for the target product (K_{NO_2}: 2; $K_{NO_3^-}$: 3);

2.5. Photo-electrochemistry

Photocurrent measurements were conducted on an electrochemical workstation (Zennium Pro, Zahner, Germany) with a gold mesh as the counter electrode, Ag/AgCl as the reference electrode, and Na_2SO_4 (0.5 M) aqueous solution as the electrolyte. Spreading a slurry of 15 mg of samples, 10 μL of PEDOT and 50 μL of water with a glass rod and using adhesive tapes as spacers on FTO glass created the work electrodes (1.0 cm^2). The photoelectrodes were dried at 50 °C for 30 minutes after drying in air.

2.6. Theoretical calculations

The density-function-theory (DFT) calculations were performed using a Quantum ESPRESSO software. The Perdew−Burke−Ernzerhof (PBE) exchange-correlation functional and the projector augmented-wave (PAW) were applied. Spin-polarization was considered for all the DFT calculations. The cutoff for the electron density representation was set at 411 Ry, whereas the energy cutoff for Kohn-Sham orbitals was set at 41 Ry. The Brillouin zone integration was carried out using the Gaussian special point approach and a smearing parameter of 0.02 Ry,. The Monkhorst-Pack k-point mesh has a density of 4 × 4 × 2.

CTO (10.81 × 11.01 × 15.38 Å) has been adopted in its ideal cubic structure with a *Pm-3m* symmetry and cubic unit cell of CTO has been extended to a 2 × 2 × 2 supercell. The periodic boundary conditions were applied to the model structure in the geometry optimization. The CTO (001) was modeled using a unit cell (10.81 × 11.01 × 20.43 Å) with a sufficient vacuum thickness (20 Å). Gas molecules (H_2O, H_2, NO, NO_2, and CO_2) were placed on the CTO (001) to simulate the gas adsorption. The adsorption energy (E_{ads})

was calculated using the following equation:

$$E_{ads} = E_{(gas\ molecule)\ +\ substrate} - E_{substrate} - E_{gas\ molecule} \quad (4)$$

where $E_{(gas\ molecule)\ +\ substrate}$, $E_{substrate}$ and $E_{gas\ molecule}$ represent the total energy of the CTO system after gas molecule adsorption, energy of the CTO system before adsorption, and energy of the gas molecule before adsorption, respectively.

3. Results

3.1. Photochromism of CTO under illumination

The XRD pattern of CTO (Figure S3) matched well that of the standard perovskite spectrum (JCPDS NO.42-0423) [23]. There was no discernible difference between the SEM images of CTO-300 and CTH-500. Apart from the band-band transition of CTO, an A_{482} could be observed in the UV-Vis spectra of as-prepared CTO (Figure 1 (a)), and was enhanced significantly in CTO-500 (Figure S5 and Figure 1 (b)). After the photocatalysis for NO oxidation under wet air (21% O_2, 1 ppm NO, 3% H_2O), the A_{482} in CTO was dependent on the [CO_2] in air: *i.e.* the A_{482} in CTO under 0 ppm CO_2 was much lower than the one under 300 ppm. Similarly, the photochromism of CTH-500 (Figure 1 (c)) revealed a significantly lower A_{482} under 50 ppm CO_2 than the one under 300 ppm CO_2. However, the reduction in 5% H_2 could elevate the production of Ti^{3+} and V_O [24], but the suppressed at the A_{482} in CTH-500 (Figure 1 (d)) suggesting that neither V_O nor Ti^{3+} was responsible for the light absorption in this band. The UV-Vis spectra of the representative CTO-300 (Figure S5 (e-f) and Figure 1 (d)) after the illumination without or with NO indicated that the presence of 1 ppm NO had no effect on photochromism, denoting that CO_2 was more important than H_2O, NO, and V_O for photochromism.

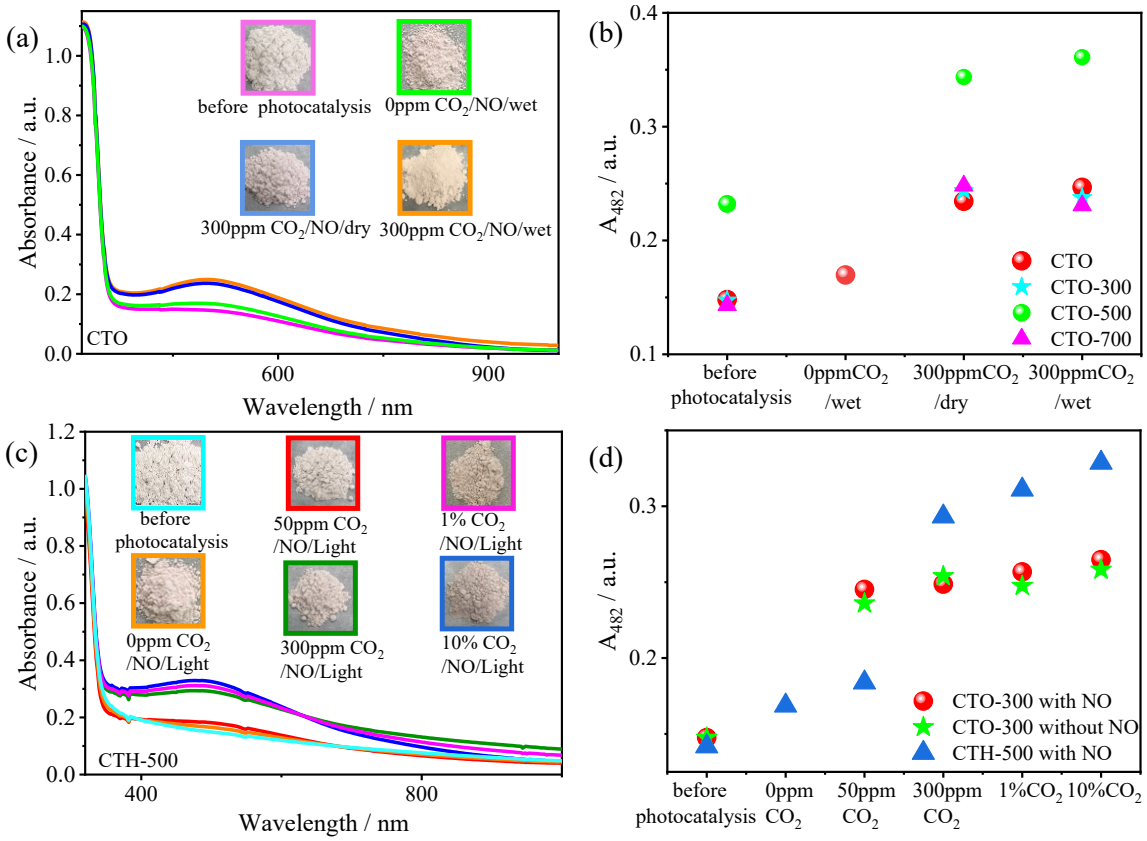

Figure 1 (a) UV-Vis spectra and CTO image before and after the photocatalytic NO oxidation; (b) A_{482} of CTO, CTO-300, CTO-500 and CTO-700 before and after photocatalysis under different conditions; (c) UV-Vis spectra and CTH-500 image after NO photocatalysis under the wet air with different [CO_2]; (d) A_{482} of CTO-300 with or without NO, CTH-500 with NO at A_{482} before and after photocatalysis under wet air with different [CO_2]; The borderline of the image of each sample indicated its color of the UV-Vis curve.

The Raman spectra of CTO-300 and CTH-500 (Figure 2 (a)) in the range of 100 to 800 cm^{-1} were attributed to the lattice vibration of perovskites [25]. In particular, the P_1 (653.2 cm^{-1}) was assigned to the Ti-O symmetrical tensile vibration mode, and the two minor subpeaks of P_1 revealed the coexistence of <TiO_6> and <TiO_5> clusters [25]. P_2 (1084.0 cm^{-1}) and P_3 (1583.0 cm^{-1}) were attributed to calcium carbonate [26] and the G band [27] produced by C-C stretching, respectively. As a result of the generation of nitrite species during NO oxidation after the photocatalysis, a peak for the NO_2^- stretch [28] formed at

874 cm^{-1} in the FTIR (Figure 2 (b)) of CTO-300 and CTH-500. The two distinct peaks at 1412 cm^{-1} and 1487 cm^{-1} were assigned to HCO_3^- and *m*-CO_3^{2-} [29], respectively, which were intensified following the photocatalysis under the wet air. The distinct CO_2 emission for HCO_3^- (300-400 °C) [30], *b*-CO_3^{2-} (400-520 °C), and *m*-CO_3^{2-} (520-700 °C) [31] can be found (Figure 2 (c)), and those for HCO_3^- and *m*-CO_3^{2-} increased after the photocatalysis, which were consistent with the FTIR data. The *b*-CO_3^{2-} of CTO-300 disappeared after the photocatalysis, because it can react quickly with H^+ for the production of HCO_3^- [32], whereas *m*-CO_3^{2-} reacted relatively slowly with H^+. The CO_2 on the surface of CTH-500 cannot form *b*-CO_3^{2-}, as *b*-CO_3^{2-} can be actively hydrogenated [33] to produce HCO_3^-. H_2 was not found in CTO-300 before or after the photocatalysis (Figure 2 (d)), but H_2 can be detected in CTH-500 and was more evident after the photocatalysis, suggesting that more hydrogenation was obtained when CTH-500 was illuminated under the wet air [34]. H^+ may move quickly to the neighboring unoccupied V_O to form a more stable structure [35], demonstrating that H_2 was not necessary for the photochromism since CTH-500 and CTO-300 showed photochromism during the photocatalysis.

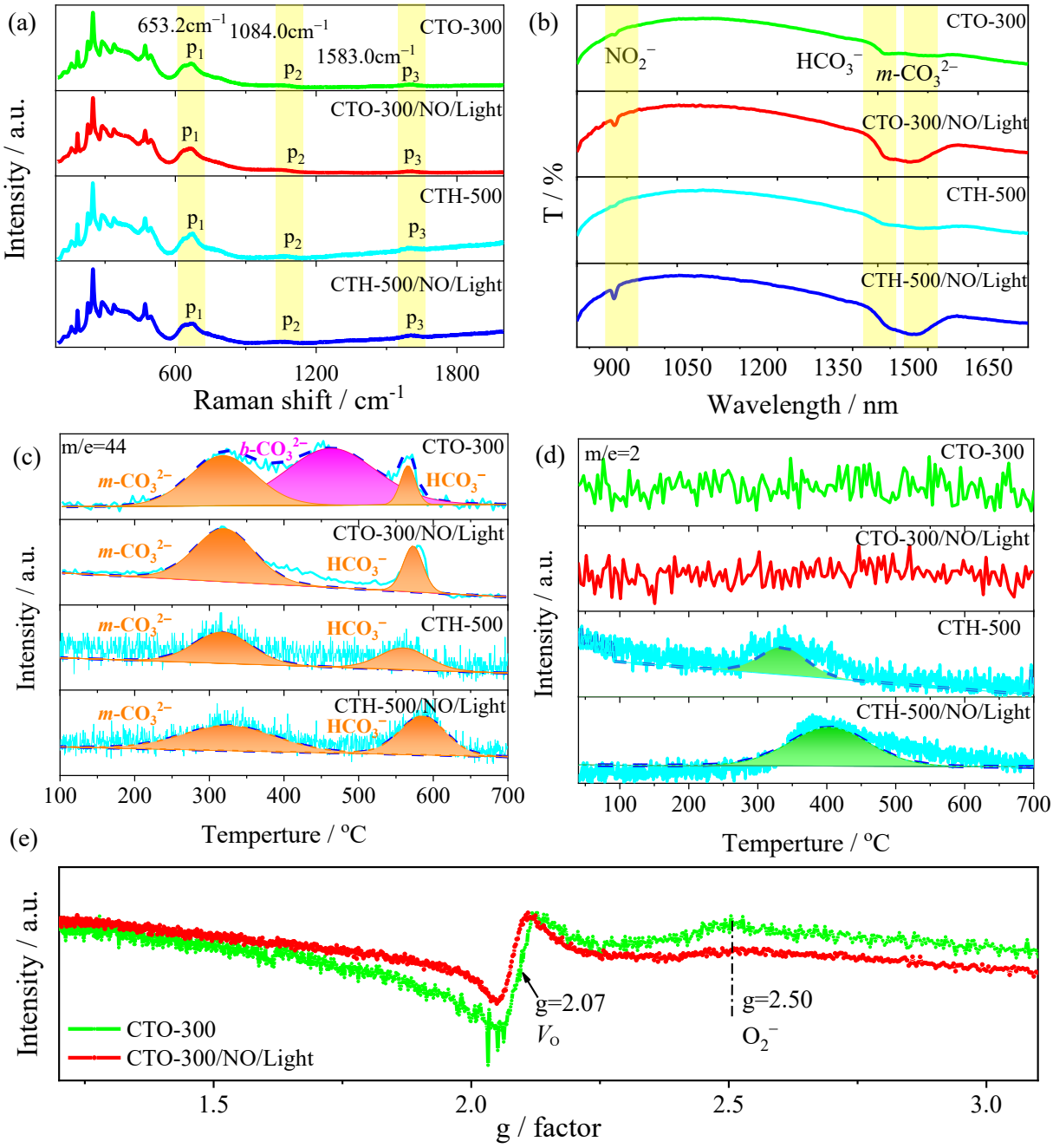

Figure 2 Raman spectroscopy (a), FTIR (b), (c) CO_2 and (d) H_2 desorption of CTO-300 and CTH-500 before and after the photocatalysis; (e) EPR of CTO-300 before and after photocatalysis in air.

The EPR signal of CTO-300 (Figure 2 (e)) before light irradiation was stronger than after light irradiation, confirming the presence of V_O (g = 2.07) [36, 37], which was consistent with the coexistence of

<TiO_6> and <TiO_5> clusters in the Raman spectroscopy. The oxidation of the CTO-300 during light irradiation reduced the signal intensity, ruling out the possibility that the photochromism was induced by the V_O. The signal of g =2.50 was produced by the adsorption of atmospheric oxygen accommodated in the surface V_O to O_2^- [38, 39]. The lower activation energy (E_a) (Figure S6) between 300 and 500 ºC than the one above 500 ºC in the conductivity measurement was due to the existence of Ti^{3+}-O-Ti^{4+} transition while the exceptionally low E_a (0.10 eV) below 300 ºC could be attributed to the presence of surface water or minor charge carriers as a result of chemical adsorption.

TGA of the photocatalysts (Figure S7) under air flow condition revealed that the weight of CTO and CTO-300 gradually increased at the temperature of 150 ºC due to O_2 adsorbed on their surface V_O. The sudden weight loss at 600 ºC may be owing to CO_2 desorption (Figure 2 (d)). The weight of CTH-500 decreased attributable to the desorption of H_2 and CO_2 was responsible for the weight loss of CTH-500 (Figure S6) at 300 and 600 ºC (Figure 2 (d, e)). Because of the decreased V_O and increased CO_2 adsorption, the final weight loss of CTO, CTO-300, and CTH-500 was larger after the photocatalysis.

The core-level scan of O 1s in XPS (Figure 3 (a)) revealed three peaks for the lattice oxygen, V_O, and •OH [40] at 529.5 eV, 531.3 eV, and 532.2 eV, respectively. The peak for •OH in CTO-300 and CTH-500 increased after the photocatalysis because water was activated to form •OH during the photocatalysts [41]. The V_O peaks of CTO-300 and CTH-500 decreased after the photocatalysis, which was consistent with the results in EPR. Furthermore, the CTO-300 of C 1s (Figure 3 (b)) peaks at 284.8 eV, 285.7 eV, and 289.6 eV were C-C, C-O-C, and C-O=C peaks, respectively [42]. CTO-300 showed a greater C-O=C concentration in XPS than CTH-500, because the *b*-CO_3^{2-} adsorbed on the surface of CTH-500 had been hydrogenated. After the photocatalysis, the C-O-C content of CTO-300 and CTH-500 increased, implying

an increased CO_2 molecule concentration on the surface of the sample after the photocatalysis in air.

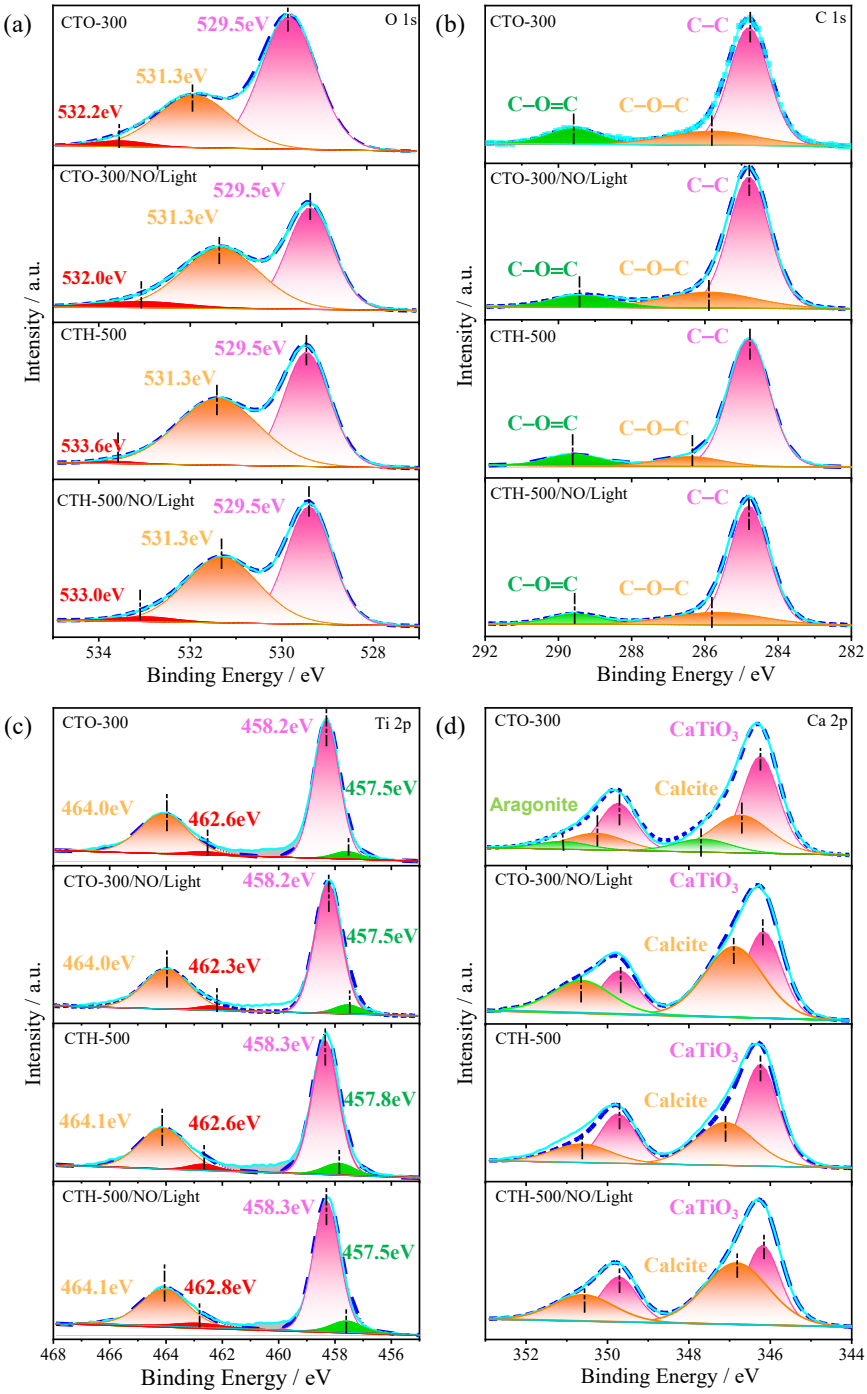

Figure 3 XPS of CTO-300 and CTH-500 before and after the photocatalysis: (a) O 1s; (b) C 1s; (c) Ti 2p; (d) Ca 2p. The photocatalysis was measured under wet air containing 300 ppm CO_2 and 1 ppm NO.

The Ti 2p peaks of CTO-300 (Figure 3 (c)) boasted Ti^{4+} 1/2p (458.2 eV), Ti^{3+} 1/2p (457.5 eV) [43,

44], and the Ca 2p peaks (Figure 3 (d)) were composed of $CaTiO_3$ (346.2 eV), calcite (346.9 eV), and aragonite (347.0 eV) [45]. CTH-500 contained more Ti^{3+} than CTO-300, and their Ti^{3+} content decreased during the photocatalysis. N element was not detected by XPS (Figure S8 (b)), which proved that neither NO nor NO_2 were crucial for the photochromism. CTO-300 and CTH-500 had a valence band (VB) position at 2.0 eV and 1.94 eV, respectively. CTO, CTO-300, and CTH-500 flat-band potentials were 0.40 eV, 0.45 eV, and 0.45 eV versus Ag/AgCl reference, respectively (Figure S9 (a)). The little difference in VB or flat band suggested that the photochromism was restricted to the oxides' surfaces.

3.2. Photocatalytic activity

The generation of reactive radical was measured using EPR to probe the photocatalysis under visible light. The peak intensity of $\bullet O_2^-$ was higher in CTH-500 than in CTO-300 (Figure S10 (a)) due to the CTH-500 surface contained more V_O, allowing more active sites for the reduction of dissolved oxygen molecule in the electrolyte. On the other hand, CTO-300 was slightly better in •OH generation, because the intermediate state near the VB caused by CO_2 adsorption on the surface of CTO-300 (Figure S10 (b)) would increase the excited h^+ under visible light from the valence band.

CTO, CTO-300, CTO-500, CTO-700, and CTH-500 showed 100% S_i under an LED lamp with photons > 400 nm (Figure S11) in dry air conditions (Figure 4 (a)), revealing the production of reactive oxygen species (ROS)for the NO oxidation reaction [46]. CTO-300, on the other hand, showed higher S_i and η than CTO-500 and CTO-700 in wet air (Figure 4 (b), Figure S11) when water molecules were involved in the photocatalysis. The η of CTO-300 decreased significantly along with the photocatalysis duration, which can be attributed to the annihilation of V_O in the presence of water molecules (Figure 2 (c)). The A_{482} was proportional to the η and AQE in the absence of water (Figure 4 (c)). The η and S_i of CTH-

500 were higher in dry air than the one in wet air (Figure 4 (d), Figure S11). Based on the above results, it was evident that NO_2 production was difficult in the absence of water.

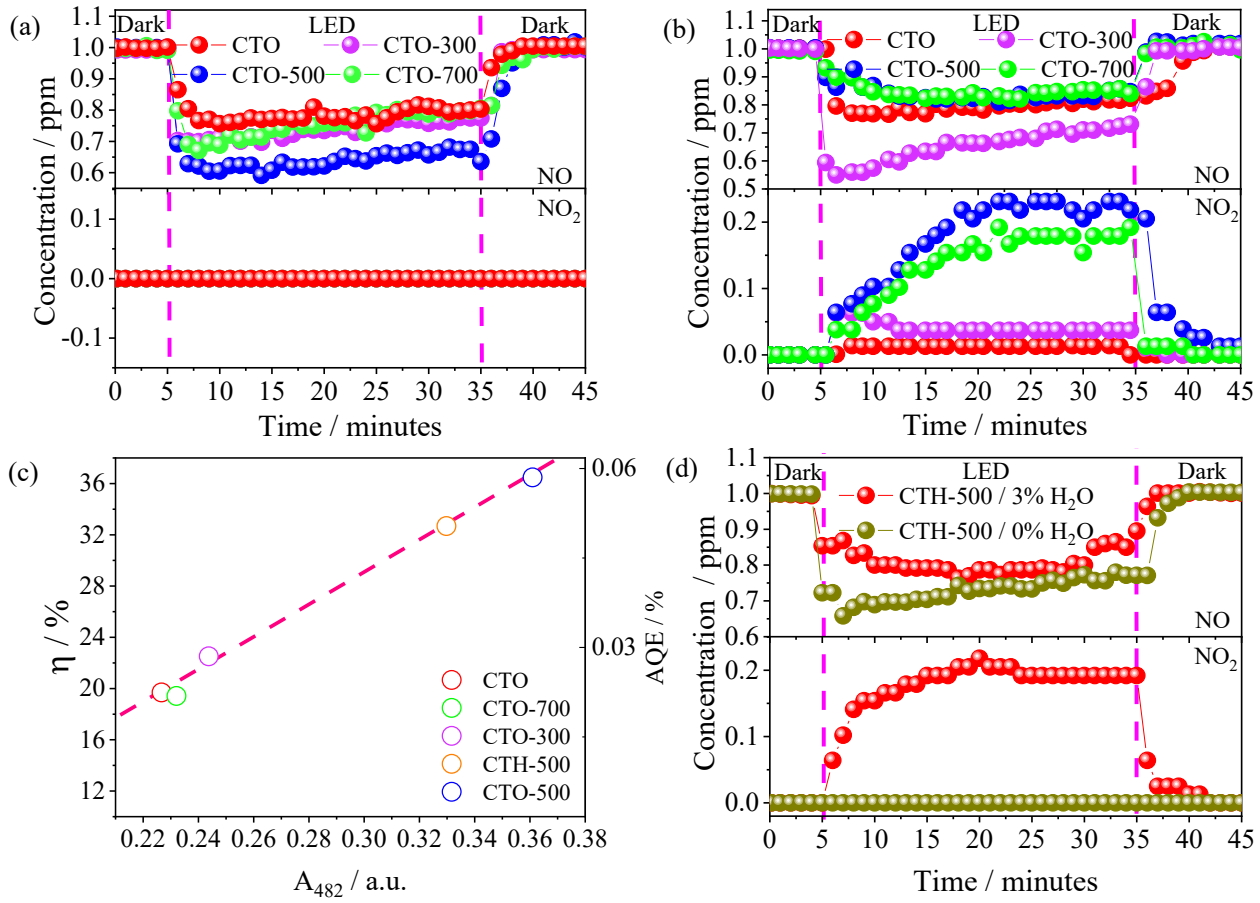

Figure 4. NO and NO_2 concentration in the photocatalytic NO oxidation over CTO, CTO-300, CTO-500, and CTO-700 under dry air (a) and wet air (b) containing 300 ppm CO_2 under LED ($\lambda > 400$ nm); (c) The relationship between the absorbance of the catalyst at 482 nm and the η at 30 minutes' illumination and maximum AQE of CTO, CTO-300, CTO-500, CTO-700, and CTH-500 under dry air and LED ($\lambda >$ 400 nm); (d) NO and NO_2 concentration over CTH-500 flowing wet or dry air under LED ($\lambda > 400$ nm); The dashed line in (c) was for the visual guide.

The assignment of the corresponding absorption bands in the *in situ* DRIFTS was summarized in Table S1. Because of the increased NO activation for the generation of NO_3^- (991 cm^{-1}) when CTO-300 was illuminated under dry air [47], the adsorbed NO (1073 cm^{-1}) gradually diminished (Figure 5 (a)) under illumination. On the contrary, the adsorbed NO significantly increased when CTO-300 was illuminated under wet conditions due to the activation of H_2O, resulting in the transformation of NO.

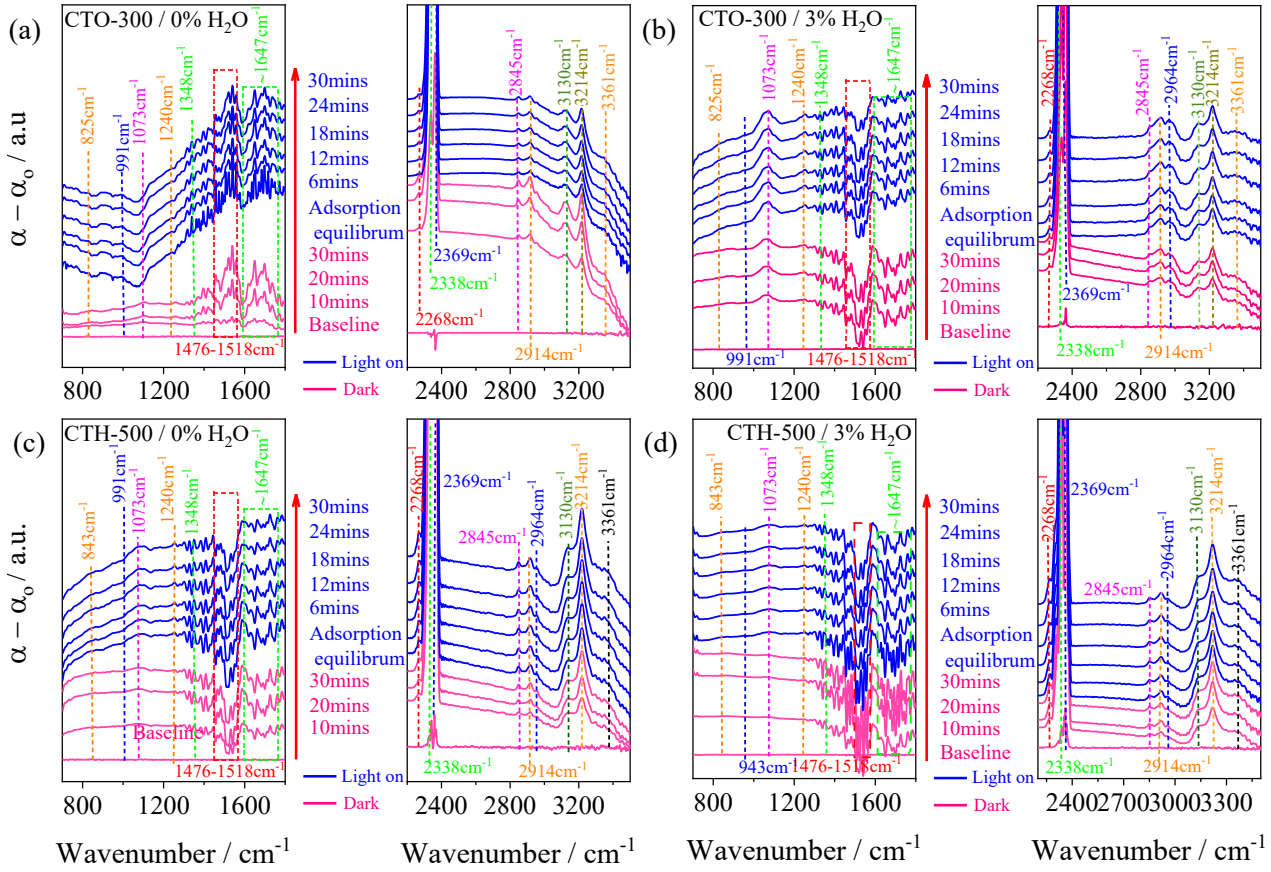

Figure 5 *In situ* DRIFTS of CTO-300 without (a) or with 3% H_2O (b) and CTH-500 without (c) or with 3% H_2O (d). The baseline was taken after the sample was sept at He flow at 110 ºC for 30 minutes and the sample was equilibrated in darkness or illumination under 40% He (dry or wet), 30% NO, and 30% air without heating.

The adsorption of CO_2 (2338 cm^{-1}, 2369 cm^{-1}) [48] following the He-sweeping surface at 110 °C under dry conditions increased with the addition of air, creating *m*-CO_3^{2-} (1476–1581 cm^{-1}) [29] and HCO_3^- (~ 1647 cm^{-1}) (**Scheme S1**) [49]. When CTO-300 was exposed to dry circumstances (40% He, 30% NO, and 30% air), *m*-CO_3^{2-} and HCO_3^- increased under dark condition and slightly decreased under illuminated condition as they were activated for the generation of CH_4 (2914 cm^{-1}) and CH_2OH (2845 cm^{-1}) [50]. However, for the CTO-300 at the wet conditions, the content of *m*-CO_3^{2-} and HCO_3^- decreased as a result of the competing adsorption of H_2O, accompanied by the appearance of a new band at 2964 cm^{-1} for HCHO. The adsorbed NO on CTH-500 continuously increased under dry or wet conditions with the introduction of NO containing gas, and the adsorption of CO_2 increased in the darkness, while the peaks for *m*-CO_3^{2-} and HCO_3^- turned out to be negative under or wet dry condition due to the production of CH_4, CH_3OH and HCHO intermediate. The carbonate bands decreased with the addition of NO-containing gas, suggesting that NO may have a stronger affinity for CTH-500 than CO_2. Obviously, •OH (3000-3400 cm^{-1}) could be found on the surface of CTO-300 and CTH-500, and their intensity enhanced with the presence of moisture.

3.3. Heterojunction with CuO or Fe_2O_3

Because of the narrow E_g of CuO (E_g = 1.7 eV) and Fe_2O_3 (E_g = 2.1 eV), the CTO/CuO or CTO/Fe_2O_3 combination naturally boosted the visible light absorption (Figure 6 (a) and Figure S12 (a)). The η of CTO/CuO mixture depended on the calcination temperature and the loading of CuO. The highest η was produced by calcining CTO with 0.25% CuO loading at 300 °C (0.25% CTO/CuO-300 (Figure 6 (b)).

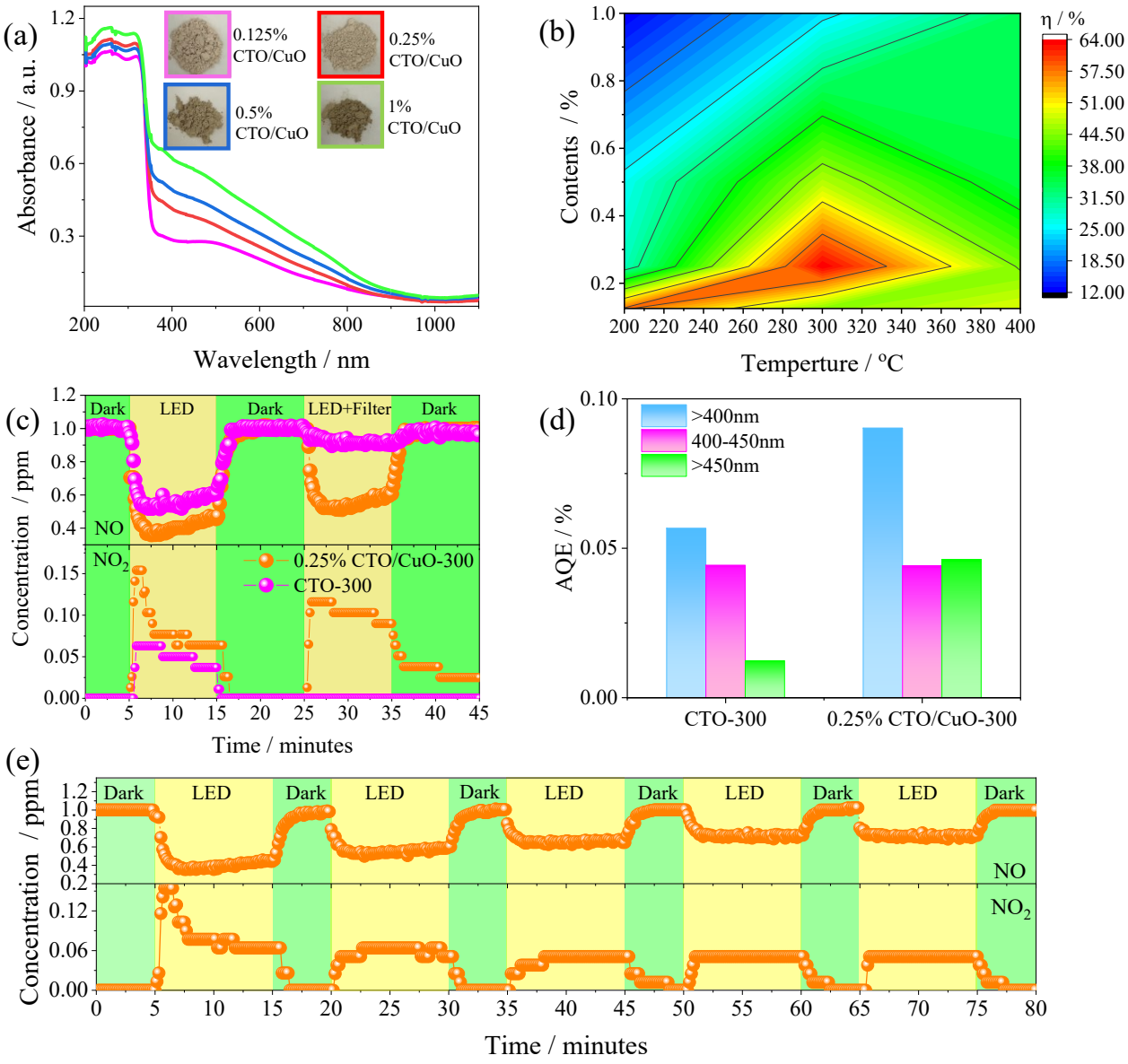

Figure 6. (a) UV-Vis spectra and image of CTO with different amount of CuO after the calcination at 300 ℃; (b) The η as a function with CuO content and calcination temperature under LED (λ > 400 nm); (c) [NO] and [NO_2] during the photocatalytic NO oxidation over 0.25% CTO/CuO-300 and CTO-300 under LED without (λ > 400 nm) and with filter (λ > 450 nm); (d) AQE of CTO-300 and T% CTO/CuO-300 under λ > 400 nm, 400nm < λ< 450nm, and λ > 450 nm; (e) Cyclic test of 0.25% CTO/CuO-300 under LED (λ > 400 nm).

When a filter was used to eliminate photons < 450 nm, the η of 0.25% CTO/CuO-300 was 40% (Figure 6 (c)). In comparison, after adding the filter, the η of CTO-300 dropped to 9.7%. What's more, the AQE of the 0.25% CTO/CuO-300 was 0.090% ($\lambda > 400$ nm) and 0.046% ($\lambda > 450$ nm), which was higher than that of CTO-300 (0.056% ($\lambda > 400$ nm) and 0.012% ($\lambda > 450$ nm)) (Figure 6 (d)), indicating that CuO was important for hot exciton generation using photons at longer wavelength. Continuous and cyclic photocatalysis (Figure 6 (e)) revealed that 0.25% CTO/CuO-300 maintained the final η above 40%. The η of CTO/Fe_2O_3 heterojunction was still poor (Figure S12 (b)): The addition of Fe_2O_3 reduced the performance of CTO on its own.

4. Discussions

The E_{ads} values of the five gases in Ti-O layer revealed that CO_2 exhibited a much higher affinity than other gases [32] (Figure 7 (a)). In reality, V_O in perovskite was demonstrated to greatly improve the adsorption affinity of NO and NO_2 [51] (Table S2), while its impact on the adsorption of H_2O, H_2 and CO_2 was less pronounced. Additionally, it was stated that CO_2 preferred to adsorb on a single Ti-O layer instead of a Ca-O layer. The Ti atoms in CTO and the orbital electrons of C and O atoms in CO_2 were hybridized (Figure 7 (b)). The results obtained from the projected density of states (PDOS) were consistent with the small extent of photochromism observed in CTH-500 in 0 and 50 ppm CO_2 with 3% H_2O, suggesting that the contribution of chemisorption H_2O was insignificant for the A_{482} and that the CO_2 molecule was paramount for photochromism.

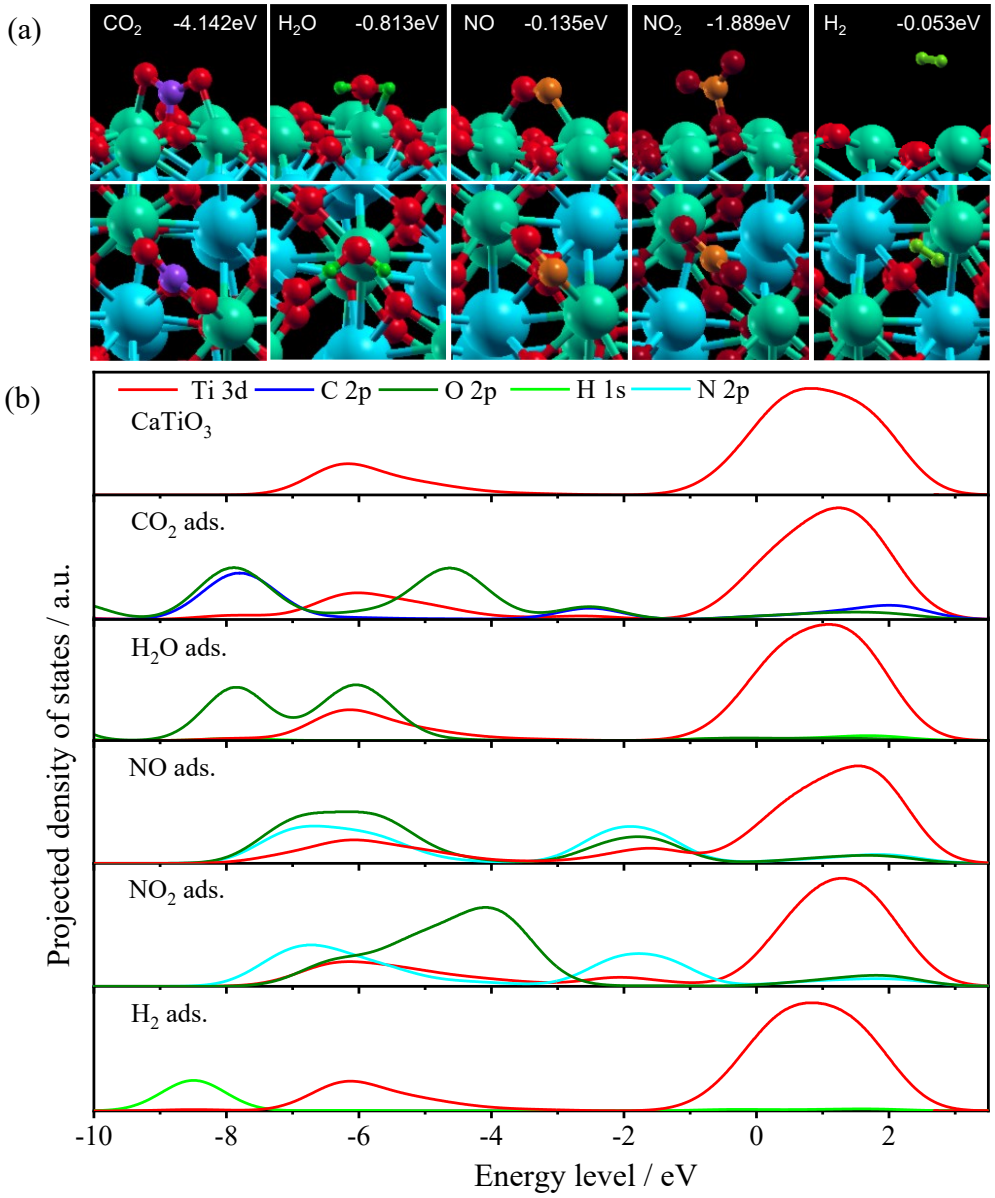

Figure 7 (a) Optimized structures of CO_2, H_2O, NO, NO_2 and H_2 on the Ti-O layer of CTO (001) without V_O. The E_{ads} after the prescreening for lowest values were given in the side views, and the E_{ads} was provided in the respective image. (b) Projected density of states (PDOS) of CTO adsorption system for five gases.

The available evidence suggested that oxygen-deficient $SrTiO_{3-\delta}$ single crystals exhibited sub-bandgap absorption at 430 nm. This photochromism was considered to be caused by the transition-metal

impurities experiencing valence change under irradiation for the production of localized chromophores [52]. These photochromic peaks, however, can be removed during calcination in a capsule containing additional SrO, a strong CO_2 getter. Furthermore, the photochromism of an oxygen-stoichiometric $SrTiO_3$ with potential Fe impurities was very weak [53], but was strongly dependent on the V_O. In accordance, we reasoned that the influence of impurities on sub band light adsorption turned out to be marginal because the impurity diversification reaction did not necessitate a change in oxygen stoichiometry.

Defects in semiconductors may induce the Urbach tail, however, the sub-band light-absorption peak could be associated with the localization of charge carriers and the binding of gas molecules or the resultant organics could change the electric field for the localization of charge carriers [54], which was mostly consistent with the observation of our present study. The emergence of these shoulder peak was typically found as a superficial doping in TiO_2 and the deep doping could evoke the shrinkage of band-to-band transition[55]: The deep level H doping TiO_2 with V_O was proposed to narrow the bandgap energy.

Combining the results of the FTIR, CO_2 desorption curves, XPS, and DRIFTS proved that the surface of the catalyst with HCO_3^- and m-CO_3^{2-} was greatly increased after the photocatalysis [56], resulting in an increase in the intensity of A_{482}. The A_{482} in CTH-500 changed more significantly than CTO-300 after photocatalysis under [CO_2] above 300 ppm, which could be attributed to more favorable CO_2 adsorption of CTH-500 with more V_O. The adsorption of CO_2 molecule on the surface of CTO-300 can reach saturation during the photocatalytic process when the [CO_2] was 50 ppm or higher.

For the oxidation of NO in air, the ubiquitous presence of CO_2 (300-400 ppm) and H_2O (1%-3%) was the critical important, because (1) H_2O was an important reactant for the production of •OH radicals, (2) they could interact with the photocatalyst along with the oxidation of NO, and (3) the liquid water layer

formed spontaneously on the catalyst surface will hinder the direct contact of NO molecule with the CTO surface [57]. Previous studies had mostly focused on the effect of H_2O as a reactant, but the involvement of CO_2 in the photocatalysis was often overlooked since the covalent double C=O bond was difficult to activate. Despite the fact that "NO_X storage" on an oxide surface has been experimentally confirmed [58], the photochromism of CTO did not change with the addition of 1 ppm NO in our case.

According to the DFT calculations, NO_2 on a V_O will spontaneously split into NO and O in the CTO lattice. However, more V_O was also beneficial to increase the adsorption of CO_2 molecules. The absorbed CO_2 could create mid-gap states to enhance the A_{482} and the photocatalyst's effect on NO oxidation in dry air was proportional to the A_{482} of the photocatalyst.

The η of CTO-300 was stronger than the other photocatalysts (CTO, CTO-500, CTO-700) under wet conditions, because H_2O and CO_2 competed with O_2 for V_O and thus the conversion of O_2 to $\bullet O_2^-$ was suppressed, reducing the η at the later stage. Therefore, CO_2 has a dichotomous effect on the photocatalytic NO abatement: The adsorption could induce the mid-gap state for enhanced visible-light adsorption while also competing with the NO or O_2 for the reactive V_O. The presence of V_O could promote the photocatalysis of water molecule for the further adsorption of H^- on the surface at ambient temperature [59] instead of activating O_2 under illumination and the desorption of H^- at low temperatures explained the production of H_2 [60]. This hindered the conversion of O_2 into $\bullet O_2^-$, thereby reducing the η. Consequently, CTH-500 displayed more efficient NO removal in dry air than in wet air.

One study suggested that that the oxidation of NO on CB will increase the production of ionic species [61], when NO combined with $\bullet O_2^-$ intermediates (Equation (5)) (Figure S10 (a)), while the oxidation of NO induced by electron holes in VB could produce gaseous NO_2 (Equation (6)):

$$4NO + 3O_2 + 2H_2O \overset{hv}{\leftrightarrow} 4HNO_3 \quad (5)$$

$$3\ NO + 2\ O_2 + H_2O \overset{hv}{\leftrightarrow} 2\ HNO_3 + NO_2 \quad (6)$$

According to the DFT calculations, the affinity of the NO_2 intermediates were enhanced greatly on the concentration of V_O and the further oxidation to produce NO_3^- (Equation (7)):

$$2NO_2 + 2H_2O + 3O_2 \overset{hv}{\leftrightarrow} 4HNO_3 \quad (7)$$

The low V_O concentration in the sample calcined at 500 and 700 °C could account for the gradual increase in NO_2 emission in wet air along with the photocatalysis.

The energy level of V_O states was 0.75 eV below the conduction band minimum (CBM) [62] in the CTO (CTO-300, **Scheme S2 (a)**). A new energy band was created above the valence band minimum (VBM) of CTO when CO_2 was adsorbed on its surface. Because neither CuO or Fe_2O_3 alone can provide only very minimum η, the synergistic η of the heterojunction between CTO/CuO heterojunction was ascribed to the *Z*-scheme charge transfer [63]. The photon-induced e^- on the CB of CuO combined with oxygen to generate $\bullet O_2^-$ which could oxidize NO to NO_3^-, while the h^+ on the VBM of CuO combined with the e^- from the CB of CTO. The reaction mechanism was illustrated in **Scheme S2 (a)** [64]. On the other hand, the CTO/Fe_2O_3 heterojunction with poor η was stipulated to under the traditional donor-acceptor transfer (**Scheme S2 (b)**) [65] due to the CBM of Fe_2O_3 was insufficient to produce reactive $\bullet O_2^-$. The distinct comparison between the two heterojunctions could imply the Z-scheme transfer of charge carriers. This *Z*-scheme charge transfer mode not only separated effectively the charge carriers [46], but also stabilized the structure of the new band and enhanced the ability to oxidize NO by using the hot excitons from CuO.

5. Conclusion

In summary, CO_2 adsorption has been demonstrated to increase the A_{482} of CTO. Different from the impurity-induced photochromism of oxygen-deficient perovskite, we found that the adsorbed CO_2 caused photochromism of oxygen deficient CTO. V_O determined the high initial η and S_i of CTO for NO abatement under wet condition due to its high affinity for NO/NO_2, but the stable photocatalysis was dependent on the photochromism after the photo-oxidation process that diminished the coupled Ti^{3+}/V_O. CO_2 could also be activated on the surface to produce hydrocarbon that altered the surface property of the photocatalyst, which was always neglected in the previous study in environmental photocatalysis. The mid-gap states created by the adsorption of CO_2 can be used to further increase the photocatalysis by creating a heterojunction with CuO through *Z*-scheme.

Acknowledgment

We would like to acknowledge the support from the National Key Research and Development Program of China (grant No. 2022YFD1601102), Natural Science Foundation of China (NSFC, 51702264, 41371275), the Fundamental Research Funds for the central universities (SWURC2020002). Funding from Chongqing Science and Technology Committee (cstc2021ycjh-bgzxm0162) is also acknowledged.CN also thanks the support of Bayu Young Scholar from Chongqing.

References

[1] S. Chen, W. Feng, H. Wang, Z. Wu, Synergistic degradation of NO and ethyl acetate by plasma activated "pseudo photocatalysis" on Ce/$ZnGa_2O_4$/NH_2-UiO-66 catalyst: Restrictive relation and reaction pathways exploration, Chem. Eng. J., 421 (2021) 129725.

[2] S. Zhao, Y. Ji, M. Jeong, H. Choe, J.W. Lee, S.Y. Kim, S. Saqlain, Z. Peng, Z. Liu, Y.D. Kim, Enhanced photocatalytic activity of TiO_2 by K incorporation towards acetaldehyde and NO oxidation: The role of K single-ion dopants and additional K-compound structures, Chem. Eng. J., 444 (2022) 136500.

[3] D.N. Mueller, M.L. Machala, H. Bluhm, W.C. Chueh, Redox activity of surface oxygen anions in oxygen-deficient perovskite oxides during electrochemical reactions, Nat. Commun, 6 (2015) 6097.

[4] C.S. Ni, J. Zhou, Z.Y. Zhang, S.B. Li, J.P. Ni, K. Wu, J.T.S. Irvine, Iron-based electrode materials for solid oxide fuel cells and electrolysers, Energy Environ. Sci., 14 (2021) 6287-6319

[5] G. Zhang, G. Liu, L. Wang, J.T.S. Irvine, Inorganic perovskite photocatalysts for solar energy utilization, Chem. Soc. Rev., 45 (2016) 5951-5984.
[6] R.R. Solis, J. Bedia, J.J. Rodriguez, C. Belver, A review on alkaline earth metal titanates for applications in photocatalytic water purification, Chem. Eng. J., 409 (2021) 128110.
[7] E. Jiang, N. Song, G. Che, C. Liu, H. Dong, L. Yang, Construction of a Z-scheme $MoS_2/CaTiO_3$ heterostructure by the morphology-controlled strategy towards enhancing photocatalytic activity, Chem. Eng. J., 399 (2020) 125721.
[8] L. Liu, Y. Jiang, H. Zhao, J. Chen, J. Cheng, K. Yang, Y. Li, Engineering Coexposed {001} and {101} Facets in Oxygen-Deficient TiO_2 Nanocrystals for Enhanced CO_2 Photoreduction under Visible Light, ACS Catal., 6 (2016) 1097-1108.
[9] D. Maarisetty, S.S. Baral, Defect engineering in photocatalysis: formation, chemistry, optoelectronics, and interface studies, J. Mater. Chem. A, 8 (2020) 18560-18604.
[10] X. Chen, L. Liu, P.Y. Yu, S.S. Mao, Increasing Solar Absorption for Photocatalysis with Black Hydrogenated Titanium Dioxide Nanocrystals, Science, 331 (2011) 746-750.
[11] X. Han, P. Liu, R. Ran, W. Wang, W. Zhou, Z. Shao, Non-metal fluorine doping in Ruddlesden–Popper perovskite oxide enables high-efficiency photocatalytic water splitting for hydrogen production, Mater. Today Energy, 23 (2022) 100896.
[12] J. Li, J. Zeng, L. Jia, W. Fang, Investigations on the effect of Cu^{2+}/Cu^{1+} redox couples and oxygen vacancies on photocatalytic activity of treated $LaNi_{1-x}Cu_xO_3$ (x=0.1, 0.4, 0.5), Int. J. Hydrogen Energy, 35 (2010) 12733-12740.
[13] H. Yu, F. Chen, X. Li, H. Huang, Q. Zhang, S. Su, K. Wang, E. Mao, B. Mei, G. Mul, T. Ma, Y. Zhang, Synergy of ferroelectric polarization and oxygen vacancy to promote CO_2 photoreduction, Nat. Commun, 12 (2021) 4594.
[14] J. Hwang, R.R. Rao, L. Giordano, K. Akkiraju, X.R. Wang, E.J. Crumlin, H. Bluhm, Y. Shao-Horn, Regulating oxygen activity of perovskites to promote NOx oxidation and reduction kinetics, Nat. Catal., 4 (2021) 663-673.
[15] Y. Peng, W. Si, J. Luo, W. Su, H. Chang, J. Li, J. Hao, J. Crittenden, Surface Tuning of $La_{0.5}Sr_{0.5}CoO_3$ Perovskite Catalysts by Acetic Acid for NOx Storage and Reduction, Environ. sci. technol., 50 (2016) 6442-6448.
[16] H.R.S. Abdellatif, G. Zhang, X. Wang, D. Xie, J.T.S. Irvine, J. Ni, C. Ni, Boosting photocatalytic oxidation on graphitic carbon nitride for efficient photocatalysis by heterojunction with graphitic carbon units, Chem. Eng. J. (Lausanne), 370 (2019) 875-884.
[17] H.S. Lim, Y. Kim, D. Kang, M. Lee, A. Jo, J.W. Lee, Fundamental Aspects of Enhancing Low-Temperature CO_2 Splitting to CO on a Double La_2NiFeO_6 Perovskite, ACS Catal., 11 (2021) 12220-12231.
[18] D. Maiti, B.J. Hare, Y.A. Daza, A.E. Ramos, J.N. Kuhn, V.R. Bhethanabotla, Earth abundant perovskite oxides for low temperature CO_2 conversion, Energ. Environ. Sci., 11 (2018) 648-659.
[19] S. Carlotto, M.M. Natile, A. Glisenti, A. Vittadini, Adsorption of CO and formation of carbonates at steps of pure and Co-doped $SrTiO_3$ surfaces by DFT calculations, Appl. Surf. Sci., 364 (2016) 522-527.
[20] S.J. Pearton, F. Ren, Y.-L. Wang, B.H. Chu, K.H. Chen, C.Y. Chang, W. Lim, J. Lin, D.P. Norton, Recent advances in wide bandgap semiconductor biological and gas sensors, Prog. Mater Sci., 55 (2010) 1-59.
[21] G.J. Meyer, The 2010 Millennium Technology Grand Prize: Dye-Sensitized Solar Cells, ACS NANO, 4 (2010) 4337-4343.
[22] K. Vikrant, K.-H. Kim, F. Dong, D.A. Giannakoudakis, Photocatalytic Platforms for Removal of Ammonia from Gaseous and Aqueous Matrixes: Status and Challenges, ACS Catal., 10 (2020) 8683-8716.
[23] N. Song, E. Jiang, X. Liu, Y. Zuo, G. Che, C. Liu, Y. Yan, H. Dong, Ni 2P QDs decorated in the multi-shelled $CaTiO_3$ cube for creating inter-shelled channel active sites to boost photocatalytic performance, J. Colloid Interface Sci., 584 (2021) 332-343.
[24] D. Cui, K. Xu, X. Dong, D. Lv, F. Dong, W. Hao, Y. Du, J. Chen, Controlled hydrogenation into defective interlayer bismuth oxychloride via vacancy engineering, Chem. Commun., 3 (2020) 1-8.
[25] L.S. Cavalcante, V.S. Marques, J.C. Sczancoski, M.T. Escote, M.R. Joya, J.A. Varela, M.R.M.C. Santos, P.S. Pizani, E. Longo, Synthesis, structural refinement and optical behavior of $CaTiO_3$ powders: A comparative study of processing in different furnaces, Chem. Eng. J., 143 (2008) 299-307.
[26] S. Martinez-Ramirez, S. Sanchez-Cortes, J. Garcia-Ramos, C. Domingo, C. Fortes, M. Blanco-Varela, Micro-Raman

spectroscopy applied to depth profiles of carbonates formed in lime mortar, Cem. Concr. Res., 33 (2003) 2063-2068.
[27] A.V. Vostrikova, E.S. Prikhozhdenko, O.A. Mayorova, I.Y. Goryacheva, N.V. Tarakina, G.B. Sukhorukov, A.V. Sapelkin, Thermal carbonization in nanoscale reactors: controlled formation of carbon nanodots inside porous $CaCO_3$ microparticles, Sci Rep, 8 (2018) 9394.
[28] J. Li, Z. Zhang, W. Cui, H. Wang, W. Cen, G. Johnson, G. Jiang, S. Zhang, F. Dong, The Spatially Oriented Charge Flow and Photocatalysis Mechanism on Internal van der Waals Heterostructures Enhanced g-C_3N_4, ACS Catal., 8 (2018) 8376-8385.
[29] J. Sheng, Y. He, J. Li, C. Yuan, H. Huang, S. Wang, Y. Sun, Z. Wang, F. Dong, Identification of Halogen-Associated Active Sites on Bismuth-Based Perovskite Quantum Dots for Efficient and Selective CO_2-to-CO Photoreduction, ACS Nano, 14 (2020) 13103-13114.
[30] W. Taifan, J.-F. Boily, J. Baltrusaitis, Surface chemistry of carbon dioxide revisited, Surf. Sci. Rep., 71 (2016) 595-671.
[31] T. Yan, N. Li, L. Wang, W. Ran, P.N. Duchesne, L. Wan, N.T. Nguyen, L. Wang, M. Xia, G.A. Ozin, Bismuth atom tailoring of indium oxide surface frustrated Lewis pairs boosts heterogeneous CO_2 photocatalytic hydrogenation, Nat. Commun, 11 (2020) 6095.
[32] J. Lin, J. Hu, C. Qiu, H. Huang, L. Chen, Y. Xie, Z. Zhang, H. Lin, X. Wang, In situ hydrothermal etching fabrication of $CaTiO_3$ on TiO_2 nanosheets with heterojunction effects to enhance CO_2 adsorption and photocatalytic reduction, Catal. Sci. Technol., 9 (2019) 336-346.
[33] H.S. Lim, G. Kim, Y. Kim, M. Lee, D. Kang, H. Lee, J.W. Lee, Ni-exsolved $La_{1-x}CaxNiO_3$ perovskites for improving CO_2 methanation, Chem. Eng. J., 412 (2021) 127557.
[34] T. Soltani, X. Zhu, A. Yamamoto, S.P. Singh, E. Fudo, A. Tanaka, H. Kominami, H. Yoshida, Effect of transition metal oxide cocatalyst on the photocatalytic activity of Ag loaded $CaTiO_3$ for CO_2 reduction with water and water splitting, Appl. Catal. B: Environ., 286 (2021).
[35] X. Liu, T.S. Bjorheim, L. Vines, O.S. Fjellvag, C. Granerod, O. Prytz, T. Yamamoto, H. Kageyama, T. Norby, R. Haugsrud, Highly Correlated Hydride Ion Tracer Diffusion in $SrTiO_{3-x}H_x$ Oxyhydrides, J. Am. Chem. Soc., 141 (2019) 4653-4659.
[36] J. Milanez, A.T. de Figueiredo, S. de Lazaro, V.M. Longo, R. Erlo, V.R. Mastelaro, R.W.A. Franco, E. Longo, J.A. Varela, The role of oxygen vacancy in the photoluminescence property at room temperature of the $CaTiO_3$, J. Appl. Phys., 106 (2009) 043526.
[37] J. Cai, A. Cao, J. Huang, W. Jin, J. Zhang, Z. Jiang, X. Li, Understanding oxygen vacancies in disorder-engineered surface and subsurface of $CaTiO_3$ nanosheets on photocatalytic hydrogen evolution, Appl. Catal. B: Environ., 267 (2020) 118378.
[38] K. Xie, N. Umezawa, N. Zhang, P. Reunchan, Y. Zhang, J. Ye, Self-doped $SrTiO_{3-\delta}$ photocatalyst with enhanced activity for artificial photosynthesis under visible light, Energ. Environ. Sci., 4 (2011) 4211.
[39] A. Kumar, M. Kumar, V. Navakoteswara Rao, M.V. Shankar, S. Bhattacharya, V. Krishnan, Unraveling the structural and morphological stability of oxygen vacancy engineered leaf-templated $CaTiO_3$ towards photocatalytic H_2 evolution and N_2 fixation reactions, J. Mater. Chem. A, 9 (2021) 17006-17018.
[40] J. Cai, M. Zhou, X. Xu, X. Du, Stable boron and cobalt co-doped TiO_2 nanotubes anode for efficient degradation of organic pollutants, J. Hazard. Mater., 396 (2020) 122723.
[41] S. Li, J. Hu, Photolytic and photocatalytic degradation of tetracycline: Effect of humic acid on degradation kinetics and mechanisms, J. Hazard. Mater., 318 (2016) 134-144.
[42] X. Zhou, W. Liu, J. Zhang, C. Wu, X. Ou, C. Tian, Z. Lin, Z. Dang, Biogenic Calcium Carbonate with Hierarchical Organic-Inorganic Composite Structure Enhancing the Removal of Pb(II) from Wastewater, ACS Appl. Mater. Interfaces, 9 (2017) 35785-35793.
[43] A. Alzahrani, D. Barbash, A. Samokhvalov, “One-Pot” Synthesis and Photocatalytic Hydrogen Generation with Nanocrystalline Ag(0)/$CaTiO_3$ and in Situ Mechanistic Studies, J. Phys. Chem. C, 120 (2016) 19970-19979.
[44] F. Xu, K. Meng, B. Cheng, S. Wang, J. Xu, J. Yu, Unique S-scheme heterojunctions in self-assembled TiO_2/$CsPbBr_3$ hybrids for CO_2 photoreduction, Nat. Commun, 11 (2020) 4613.

[45] S.W. Lee, L.M. Lozano-Sanchez, V. Rodriguez-Gonzalez, Green tide deactivation with layered-structure cuboids of Ag/$CaTiO_3$ under UV light, J. Hazard. Mater., 263 Pt 1 (2013) 20-27.
[46] H. R.S. Abdellatif, G. Zhang, Y. Tang, W. Ruan, J. Li, D. Xie, J. Ni, C. Ni, A highly efficient dual-phase GaN(O)/Nb_2O_5(N) photocatalyst prepared through nitridation and reoxidation process for NO removal, Chem. Eng. J., 402 (2020) 126199.
[47] Y. Huang, Y. Gao, Q. Zhang, Y. Zhang, J.J. Cao, W. Ho, S.C. Lee, Biocompatible FeOOH-Carbon quantum dots nanocomposites for gaseous NOx removal under visible light: Improved charge separation and High selectivity, J. Hazard. Mater., 354 (2018) 54-62.
[48] L. Ye, M. Zhang, P. Huang, G. Guo, M. Hong, C. Li, J.T. Irvine, K. Xie, Enhancing CO_2 electrolysis through synergistic control of non-stoichiometry and doping to tune cathode surface structures, Nat. Commun, 8 (2017) 14785.
[49] C. Luo, J. Zhao, Y. Li, W. Zhao, Y. Zeng, C. Wang, Photocatalytic CO_2 reduction over $SrTiO_3$: Correlation between surface structure and activity, Appl. Surf. Sci., 447 (2018) 627-635.
[50] X. Sun, J. Lin, Y. Wang, L. Li, X. Pan, Y. Su, X. Wang, Catalytically active Ir^0 species supported on Al_2O_3 for complete oxidation of formaldehyde at ambient temperature, Appl. Catal. B: Environ., 268 (2020) 118741.
[51] H. Li, J. Li, Z. Ai, F. Jia, L. Zhang, Oxygen Vacancy-Mediated Photocatalysis of BiOCl: Reactivity, Selectivity, and Perspectives, Angew. Chem. Int. Ed. Engl., 57 (2018) 122-138.
[52] J. Yao, K. Hashimoto, Fujishima, Photochromism induced in an electrolytically pretreated MoO_3 thin film by visible light, Nature, 355 (1992) 624-626.
[53] W.D. Rice, P. Ambwani, M. Bombeck, J.D. Thompson, G. Haugstad, C. Leighton, S.A. Crooker, Persistent optically induced magnetism in oxygen-deficient strontium titanate, Nat. Mater., 13 (2014) 481-487.
[54] C. Ni, G. Hedley, J. Payne, V. Svrcek, C. McDonald, L.K. Jagadamma, P. Edwards, R. Martin, G. Jain, D. Carolan, D. Mariotti, P. Maguire, I. Samuel, J. Irvine, Charge carrier localised in zero-dimensional $(CH_3NH_3)_3Bi_2I_9$ clusters, Nat. Commun., 8 (2017) 170.
[55] Y. Yang, L.-C. Yin, Y. Gong, P. Niu, J.-Q. Wang, L. Gu, X. Chen, G. Liu, L. Wang, H.-M. Cheng, An Unusual Strong Visible-Light Absorption Band in Red Anatase TiO2 Photocatalyst Induced by Atomic Hydrogen-Occupied Oxygen Vacancies, Adv. Mater. (Weinheim, Ger.), 30 (2018) 1704479.
[56] S. Yao, H. Zhang, Z. Chen, H. Lin, S. Han, X. Wu, R. Dong, Z. Wu, T. Nozaki, Promotion of graphitic carbon oxidation via stimulating CO2 desorption by calcium carbonate, J. Hazard. Mater., 363 (2019) 10-15.
[57] F. He, S. Weon, W. Jeon, M.W. Chung, W. Choi, Self-wetting triphase photocatalysis for effective and selective removal of hydrophilic volatile organic compounds in air, Nat. Commun., 12 (2021) 1-12.
[58] Y. Yoshiyama, S. Hosokawa, K. Tamai, T. Kajino, H. Yoto, H. Asakura, K. Teramura, T. Tanaka, NOx Storage Performance at Low Temperature over Platinum Group Metal-Free $SrTiO_3$ Based Material, ACS Appl Mater Interfaces, (2021) 29482-29490.
[59] K.A. Stoerzinger, L. Wang, H. Su, K.-J. Lee, E.J. Crumlin, Y. Du, Influence of strain on $SrFeO_{3-\delta}$ oxidation, reduction, and water dissociation: Insights from ambient pressure X-ray photoelectron spectroscopy, Appl. Surf. Sci., 527 (2020) 146919.
[60] S.K. Lakhera, A. Rajan, R. T.P, N. Bernaurdshaw, A review on particulate photocatalytic hydrogen production system: Progress made in achieving high energy conversion efficiency and key challenges ahead, Renew. Sust. Energ. Rev., 152 (2021) 111694.
[61] G. Dong, L. Yang, F. Wang, L. Zang, C. Wang, Removal of Nitric Oxide through Visible Light Photocatalysis by g-C_3N_4 Modified with Perylene Imides, ACS Catal., 6 (2016) 6511-6519.
[62] X. Pan, M.Q. Yang, X. Fu, N. Zhang, Y.J. Xu, Defective TiO_2 with oxygen vacancies: synthesis, properties and photocatalytic applications, Nanoscale, 5 (2013) 3601-3614.
[63] D.L. Huang, S. Chen, G.M. Zeng, X.M. Gong, C.Y. Zhou, M. Cheng, W.J. Xue, X.L. Yan, J. Li, Artificial Z-scheme photocatalytic system: What have been done and where to go?, Coord. Chem. Rev., 385 (2019) 44-80.
[64] S. Jung, K. Yong, Fabrication of CuO-ZnO nanowires on a stainless steel mesh for highly efficient photocatalytic applications, Chem. Commun. (Camb), 47 (2011) 2643-2645.

[65] L.W. Zhang, H.H. Mohamed, R. Dillert, D. Bahnemann, Kinetics and mechanisms of charge transfer processes in photocatalytic systems: A review, J Photoch. Photobio. C, 13 (2012) 263-276.